

Micromechanical Flying Insect (MFI)
Year 1 Report May 1998 — May 1999

R.S. Fearing, K.S.J. Pister, S.S. Sastry (Dept. of EE&CS)
M.H. Dickinson (Dept. of Integrative Biology)
D. Liepmann and A. Majumdar (Dept. of Mechanical Engineering)
T. Sands (Dept. of Materials Science and Engineering)
University of California
Berkeley, CA 94720-1770
phone: (510) 642-9193 email: ronf@eecs.berkeley.edu

1 Project Overview

We propose to develop a micromechanical flying insect (MFI), a 10-25 mm (wingtip-to-wingtip) device eventually capable of sustained autonomous flight. The goal of the MFI project is to use biomimetic principles to capture some of the exceptional flight performance achieved by true flies. The project is divided into four stages: 1) feasibility analysis, 2) structural fabrication, 3) aerodynamics and wing control, and 4) flight control and integration. Our design analysis shows us that piezoelectric actuators and flexible thorax structures can provide the needed power density and wing stroke, and adequate power can be supplied by solar cells. In the first year of this MURI grant, research has been concentrated in understanding fly flight aerodynamics and in analysis, design and fabrication of MFI structures.

2 MFI Feasibility Analysis and Design

As a design target for the MFI, we are using the blowfly *Calliphora* (Figure 1), which is large enough for relatively easy assembly of actuators, thorax, wings, and electronics. A set of the most relevant parameters is shown in Table 1. The first critical determination is whether enough

parameter	blowfly
total mass	$100 \times 10^{-6} \text{ kg}$
actuator mass	$\approx 50 \times 10^{-6} \text{ kg}$
wing length	11 mm
flight power	$\approx 4 \text{ mW}$
actuator power	$\approx 8 \text{ mW}$
wing mass	10^{-6} kg
wing inertia J	$20 \times 10^{-12} \text{ kg m}^2$
joint stiffness	$\approx 2 \times 10^{-5} \text{ Nm} \cdot \text{rad}^{-1}$
resonant frequency	150 Hz
wing "damping"	$\approx 10^{-8} \text{ Nms}$
quality factor Q	≈ 1

Table 1: *Calliphora* design parameters.

19990622 093

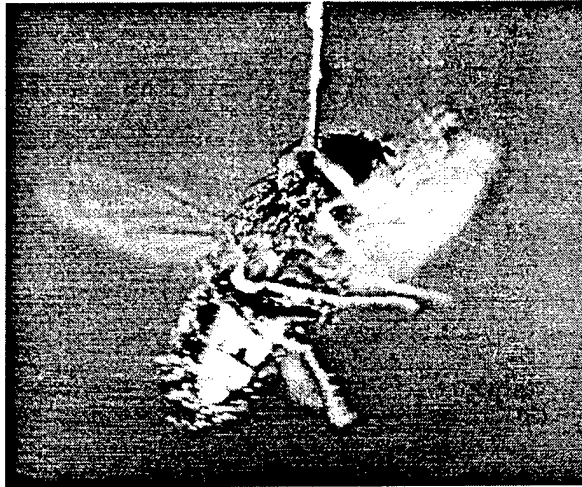


Figure 1: *Calliphora erythrocephala*

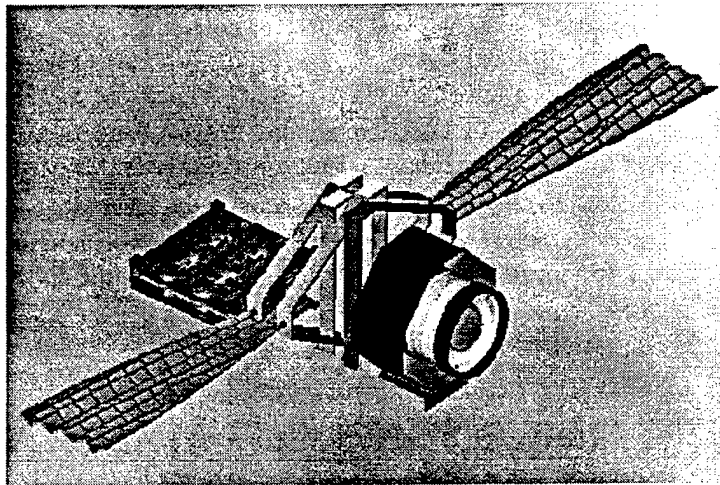


Figure 2: Current conceptual drawing of micromechanical flying insect.

mechanical power can be delivered to drive the wings. We found that the actuator mass for the MFI will be significantly less than for the blowfly as piezoelectric actuators potentially have much greater power density than muscle. The MFI has greater wing inertia for better impedance matching with the relatively stiff actuators.

Our second key design consideration is a thorax structure which can transform small piezo actuator deflections into the large wing stroke and rotation required to achieve efficient flight. As shown in Figure 2, we will be using flexural 4 bar elements to provide sufficient wing stroke, and a compliant wing which can deform to provide rotation. A summary of the MFI component dimensions is given in Table 2.

2.1 Thorax and Actuator Resonance, Q , and Power

We analyzed the MFI actuator/transmission/wing system using a resonant circuit model (Figure 3), and have refined parameter values for wing inertia, actuator stiffness, etc. as shown in

MFI component	size	quantity	mass
piezo actuator	0.25 mm by 5 mm long by 0.2mm thick	8	15 mg
thorax structure 1 mm by 1mm box beam	10 μm thick stainless, 1 mm wide,	4	20 mg
wings HEXSIL + polyimide	5 mm by 10 mm by 10 μm	2	3 mg
base frame box beam (stainless)	10 mm by 4 mm by 1 mm, 10 μm thick	1	8 mg
wiring	10 mm long by 10 μm by 10 μm	100	0.5 mg
solder bumps	100 μm diameter	200	1 mg
total structure budget			47.5 mg
electronics sensors+CPU+com+power	10 mm by 10 mm by 200 μm silicon	1	50 mg
total MFI Mass			97.5 mg

Table 2: Components of MFI.

parameter	100 Hz	150 Hz
actuator mass $lwh\rho$	$< 40mg$	$< 40mg$
max. stiffness K_{SL}	$100Nm^{-1}$	$230Nm^{-1}$
min. force F_{SL} ($B_{SL} \approx B_L$)	59 mN	59 mN
min. force F_{SL} ($B_{SL} \ll B_S$)	29 mN	29 mN
wing damping B_L	$9.4 \times 10^{-2} Nsm^{-1}$	$6.4 \times 10^{-2} Nsm^{-1}$
wing amplitude	$\theta = 1$ radian	$\theta = 1$ radian
required power	$4.6 \times 10^{-3} W$	$7.0 \times 10^{-3} W$
wing pulley radius r	0.5 mm	0.5 mm
wing inertia	$12 \times 10^{-12} < J < 60 \times 10^{-12} kgm^2$	$12 \times 10^{-12} < J < 60 \times 10^{-12} kgm^2$
load mass M_L	$0.5 \times 10^{-4} < M_L < 2.5 \times 10^{-4} kg$	$0.5 \times 10^{-4} < M_L < 2.5 \times 10^{-4} kg$

Table 3: Model assumptions and parameter limits for MFI, with load parameters transformed into translational domain.

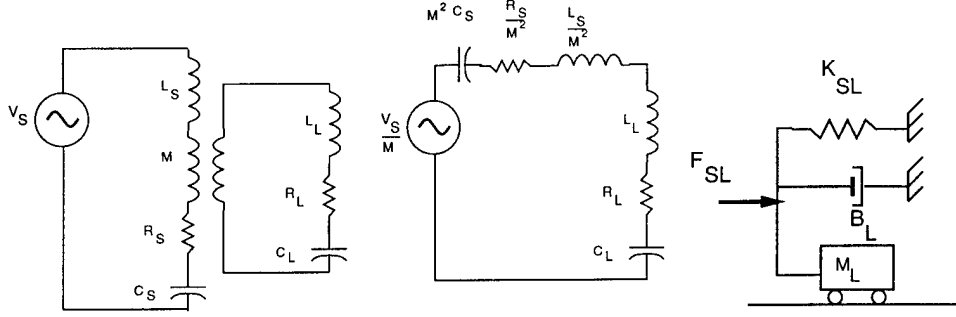


Figure 3: Electrical and mechanical equivalent resonant models for actuator, thorax, and wing. The actuator can be modelled as a voltage (force) source with equivalent damping (R_S), stiffness (C_S^{-1}), and inertia (L_S). The thorax is modeled as a transformer with coupling ratio M , and the wing-hinge combination (the load) has damping (R_L), stiffness (C_L^{-1}), and inertia (L_L). Typically, for unmatched piezo and load impedances, the stiffness of the actuator is much greater than the load stiffness, and the actuator damping is much less than the equivalent wing damping. Hence the efficiency is close to 100% but the power density is quite low compared to matched conditions.

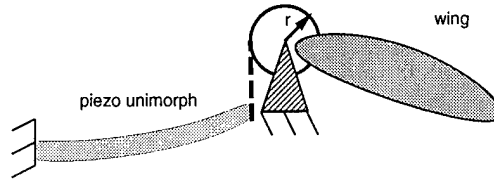


Figure 4: Mechanical schematic of actuator and wing connection. Virtual pulley represents thorax kinematics and motion amplification.

Table 3. We found that actuator stiffness is one of the key limitations in the design, as excessive wing inertia is required to resonate a stiff actuator. Parameter limits for the transformed actuator force F_{SL} and actuator damping B_{SL} are given in Table 3, for the high efficiency (load damping much greater than actuator damping) and high power density (load damping equal to actuator damping) cases.

We developed a simple mechanical model of the MFI using a cantilever actuator (which gives larger stroke at less force than a bulk-type actuator). Through the principle of virtual work, the exact form of the thorax motion amplification is not needed for power calculations, and is shown as a simple pulley in Figure 4. Using the resonant circuit model of Figure 3, we analyzed power requirements and wing stroke amplitude assuming a piezoelectric unimorph (Figure 4). We obtained design parameters as given in Table 4, using an actuator $5 \times 0.2 \times 2mm^3$ in size. A 15 mg mass of PZT5H can generate more than the 7 mW of mechanical power required at a frequency of 150 Hz. Calculations show the efficiency is better than 95%. Note that this is the total actuator volume required for both wings. Also note that the actuator is stiff compared to muscle, resulting in a higher Q and high efficiency but low power density. (The quality factor Q is the ratio of stored energy to the energy dissipated per radian of the wing stroke cycle.) This actuator is limited by its strength to peak tensile strains less than 0.1%. The wing power and amplitude for this model are shown in Figure 5. Our analysis of single-crystal piezo materials such as PMNPT shows even better performance, but fabrication would be more difficult.

parameter	value
frequency ω	$2\pi 150 \text{ sec}^{-1}$
high E mechanical Q	≈ 10
material stiffness Y_{11}	$8.2 \times 10^{10} \text{ Nm}^{-2}$
ideal actuator power density	1.5 kW kg^{-1}
actuator dimensions lwh	$5 \times .2 \times 2 \times 10^{-9} \text{ m}^3$
actuator mass	$15 \times 10^{-6} \text{ kg}$
applied field E_3	$2 \times 10^6 \text{ Vm}^{-1}$
blocked force F_S	0.135 N
free displacement x_{DC}	$5.1 \times 10^{-5} \text{ m}$
resonant freq. ω_o	$4.4 \times 10^4 \text{ sec}^{-1}$
$K_S = \frac{F_S}{x_{DC}}$	2600 Nm^{-1}
$M_S = \frac{K_S}{\omega_o^2}$	$1.4 \times 10^{-4} \text{ kg}$
B_S	$.134 \text{ Nsm}^{-1}$
transmission ratio T	4.5
F_{SL}	30 mN
K_{SL}	130 Nm^{-1}
B_{SL}	$2.9 \times 10^{-3} \text{ Nsm}^{-1}$
M_{SL}	$6.7 \times 10^{-6} \text{ kg}$
required M_L	$1.4 \times 10^{-4} \text{ kg}$
wing stroke at 150 Hz	110°
wing power at 150 Hz	6.5 mW
overall Q	2.1
efficiency η	95.5%
actuator power density	400 W kg^{-1}
peak beam stress	$1.2 \times 10^8 \text{ Nm}^{-2}$
peak beam strain (compressive)	0.15%
peak beam deflection x_S	$1 \times 10^{-4} \text{ m}$

Table 4: Model assumptions for PZT5 actuation of both wings using a pre-stressed unimorph.

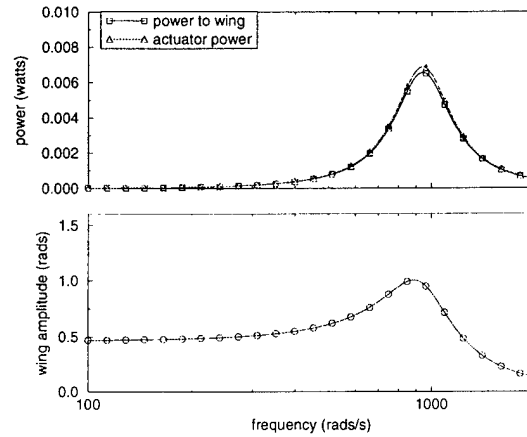


Figure 5: Wing power and wing amplitude for PZT-5H piezo unimorph.

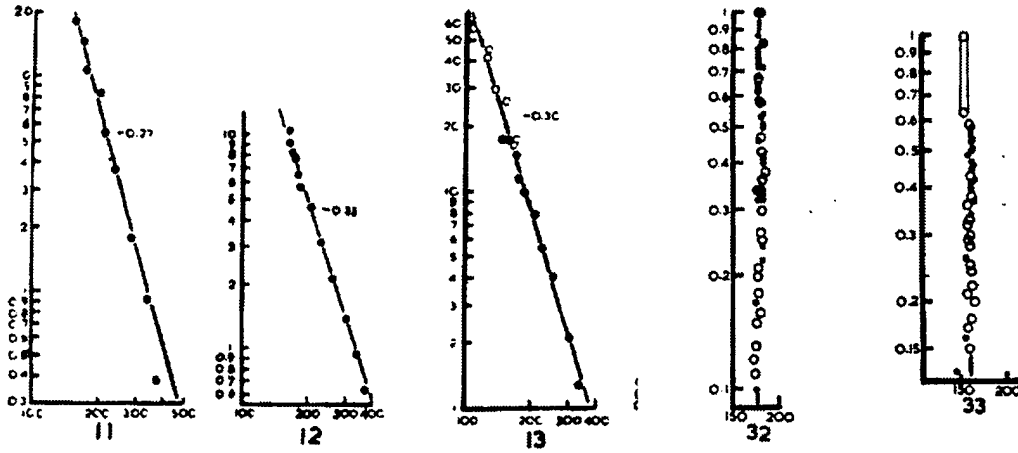


Figure 6: Blowfly resonance measurements, with change in wing inertia (11,12,13) and change in air pressure (32,33). Best fit: $\omega = \sqrt{\frac{k}{J_{wing} + J_{thorax}}}$, $J_{wing} = 4.1 J_{thorax}$. A. Sotavalta, "The Wing Stroke Frequency of Insects in Wing Mutilation and Loading Experiments at Sub-atmospheric Pressure", *Am. Zool. Soc.*, vol. 15, no. 2m pp. 1-67, 1952.

2.2 Insect Thorax Measurements and Models

The resonant thorax model for the MFI is consistent with blowfly data (Figure 6). Changing wing inertia changes the resonant frequency, while changing damping (due to reducing air pressure) has no effect on resonant frequency. We have been comparing predictions from the resonant model for the MFI with blowfly data. From published data [Sotavalta, 1952] of wing inertia and resonant frequency, we can estimate an equivalent rotational stiffness for the joint. Since the torque due to wing motion can be upper bounded by a linear damping factor B , the quality factor Q can be estimated for the real insect. Our initial conjecture was that the Q of an insect would be fairly large, to enhance wing stroke amplitude in some fashion. In fact, the data indicates that the overall Q of the wing-thorax system is rather low (about 1), and a higher Q would only increase mass, stiffness, and peak stresses, while reducing controllability without increasing wing stroke amplitude.

We started a set of experiments, using blowflies, to verify published data about the spring constant (K) of the thorax and the moment of inertia (J) of the wing. We have measured the spring constant of the wing hinge of dead *Calliphora*, found the moment of inertia for the wing, and flown the tethered animals with weight added or removed from the wings. Early results confirm the expected square root relationship between the weight of the wing and the frequency at which the animal beats its wings. The moment of inertia for a single wing is approximately $2.5 \times 10^{-11} \text{ kg m}^2$. About 75% of the weight of the wing can be found in the basal half that is attached to the hinge; thus inertia is higher at distances closer to the thorax. The wing spring constant is measured at about $2 \times 10^{-6} \text{ Nm rad}^{-1}$, which is only about one tenth the joint stiffness required for a 150 Hz resonance, considering the wing inertia of $2 \times 10^{-11} \text{ kg m}^2$. One explanation for this may be that we are measuring only the wing joint stiffness, perhaps due to the wing joint being disconnected from thorax and muscle in the dead animal.

We intend to use the implications of the low Q thorax-wing system in our MFI design. The key implications of a low Q design are:

- dynamic muscle and thorax stress is multiplied by Q , so peak stress is not significantly

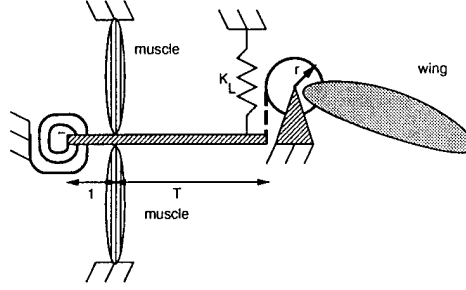


Figure 7: Model of muscle pair driving wing. Effective transmission ratio determined by lever ratio and pulley diameter.

increased.

- the forces due to inertia and stiffness are small compared to aerodynamic dissipation, which implies that wing motion is significantly affected by aerodynamic loading
- dynamic effects in the thorax are small, so wing motion is dominated by thorax kinematics and aerodynamic loading, rather than thorax dynamics.
- the resonance is fairly broad, so the insect can quickly change stroke amplitude, and start/stop wing beat

A particularly important point for our MFI design is that if stored energy is kept relatively small, we only need to consider the kinematic and quasistatic design of the thorax, rather than a coupled dynamic design. This is a much less daunting task, and amenable to more conventional mechanism design techniques.

2.2.1 Muscle Actuation

Figure 7 shows an idealized antagonist muscle pair driving a wing, through a lever arm and a wing pulley. This simple kinematics models some of the thorax mechanics but greatly neglects thorax dynamics. The muscle is of course highly non-linear, but as the insect flight muscles are operating at low strain, the linear model may provide insight into important parameters. The inertial forces of the muscle are likely negligible at resonance. As the dorsal longitudinal (DLM) and dorsal ventral muscles (DVM) drive both wings, all power and force numbers were calculated for an actuator driving both wings simultaneously.

Using blowfly muscle parameters as in Table 5, the equivalent linear parameters can be calculated assuming that the muscle damping is obtainable from $B_S = \frac{F_S^2}{4P_S}$. Note that the muscle impedance B_S is greater than the load impedance. Hence a transformer should be used to reduce the source impedance and increase power delivery to the load. In addition, the muscle stiffness would require a very large load inertia to resonate. A transmission ratio $T = 8.0$ brings these parameters into balance. The transformed force, damping, stiffness, and inertia for the muscle actuator are given by the subscript "SL". Note that after transformation, the load and source impedance is well matched with muscle, and hence half the muscle power is lost in internal dissipation. Note that the literature gives flight muscle power density as $\approx 100 W kg^{-1}$ which is the net mechanical power output at the wings. Since we assume 50% system efficiency, the muscle mechanical output is twice as much.

The power delivered to the wings is shown in Figure 8. Note that the predicted Q is quite low, so wing beat frequency can be varied with only a small change in power delivery.

parameter	value
frequency ω	$2\pi 100 \text{ sec}^{-1}$
muscle stiffness c_E	$2.5 \times 10^6 \text{ Nm}^{-2}$
muscle power density ρ_{power}	200 W kg^{-1}
muscle dimensions lwh	$5 \times 3 \times 3 \times 10^{-9} \text{ m}^3$
muscle mass	$40 \times 10^{-6} \text{ kg}$
blocked force F_S	0.45 N
free displacement X_{DC}	10^{-4} m
DC strain	0.02
K_S	$4.5 \times 10^3 \text{ Nm}^{-1}$
$M_S = \frac{lwh\rho}{3}$	$1.5 \times 10^{-5} \text{ kg}$
B_S	6.3 Nsm^{-1}
transmission ratio T	8.0
F_{SL}	60 mN
K_{SL}	70 Nm^{-1}
B_{SL}	$9.9 \times 10^{-2} \text{ Nsm}^{-1}$
M_{SL}	$0.2 \times 10^{-6} \text{ kg}$
required M_L	$1.8 \times 10^{-4} \text{ kg}$
wing stroke at 100 Hz	107°
wing power at 100 Hz	4 mW
overall Q	1.2
efficiency η	49%

Table 5: Model assumptions for muscle actuation of both wings together.

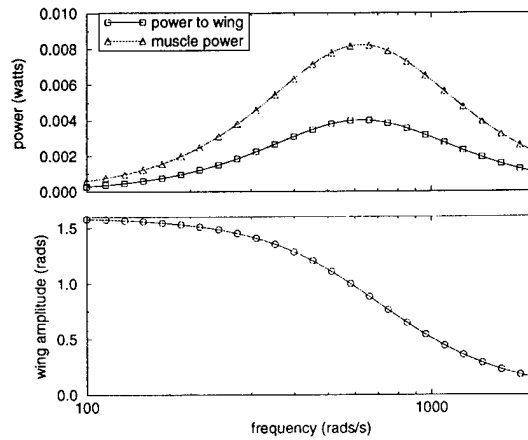


Figure 8: Total wing power and wing amplitude for muscle actuation, with resonance at 100 Hz.

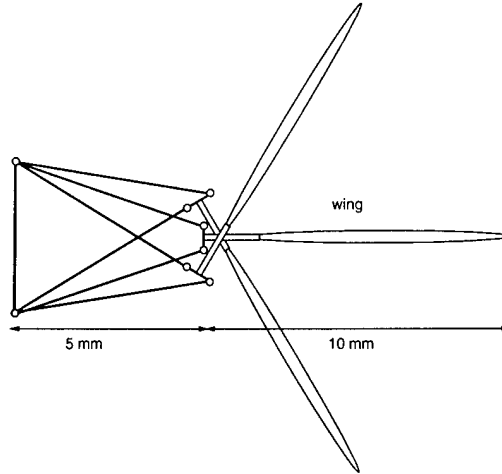


Figure 9: Rigid link kinematic model of 4 bar mechanism capable of 120° stroke angle.

3 Structural Fabrication

We have preliminary designs for the thorax and wings, and have identified appropriate processes for piezo actuator fabrication and attachment.

3.1 Thorax Design

A key design issue for the MFI is creating a transmission system to convert small-strain high-force actuators such as piezoelectric unimorphs to large amplitude wing deflections and rotation. Finding a good kinematic structure to provide sufficient wing pronation/supination has been challenging. Our current plan is to use two 4 bar planar mechanisms for each wing. with a fan-folded wing as in Figure 2 to get adequate wing rotation. We chose a 4 bar design to give 120° wing stroke with $\pm 10^\circ$ actuator stroke, as shown in Figure 9. Currently, $10\mu\text{m}$ thick stainless steel sheet looks quite promising for building the thorax frames. The stainless steel can be folded into beams for rigid links and bent into flexures for joints. Each frame will be about 6 mm long, and weigh about 5 mg, for a total thorax mass of 20 mg, allowing up to 30 mg for piezo actuators. We made our first generation structure using folded stainless steel sheet, $25\mu\text{m}$ thick, fabricated using a photoetching process, at $10\times$ scale for easy assembly (Figure 10). We need to improve joint lateral stiffness (probably using split-tube flexures) and wing mounting points in the next generation parts.

We have mounted large-scale THUNDER actuators from Face International Corp. on our flexural structures, and seen 10° of actuator motion at resonance. These actuators are a piezoelectric unimorph which is pre-stressed such that the ceramic material is always under compression. Bimorph power limits are determined by the maximum tensile stress of the actuator, which limits peak strains to the order of 0.1%. Although a unimorph has only half the displacement and half the force of a bimorph of the same dimensions, it can be used with 10 times the applied field, since the piezo remains in compression. The pre-stressed unimorph can then have 25 times the power density of a bimorph. We have thus changed our designs to use pre-stressed unimorphs rather than bimorphs for wing actuation.

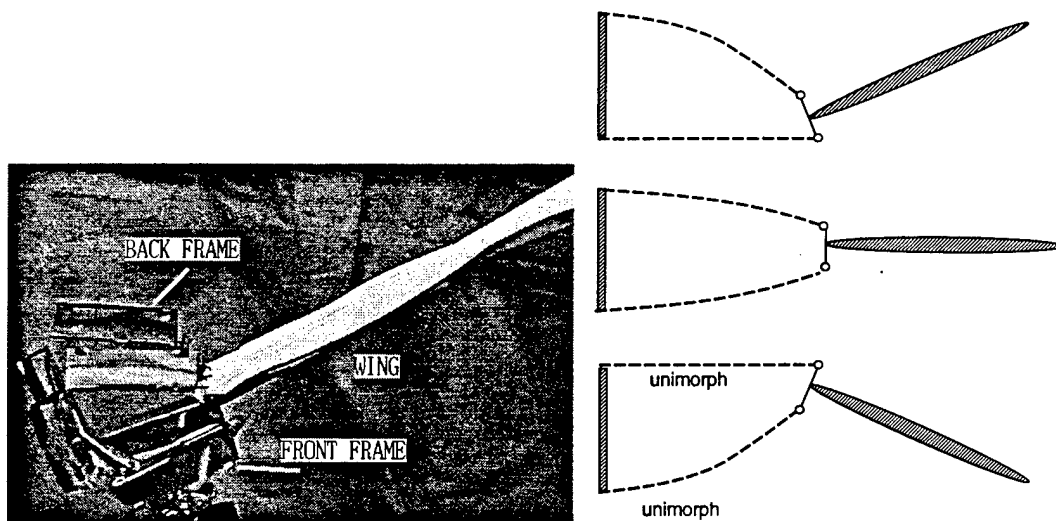


Figure 10: Large scale (10 \times) prototype thorax using two driven frames, with wing mounted on flexure between two frames. Frames are made from folded 25 μ m stainless. In this design, each wing moves independently, with two actuators per frame, and two frames per wing. Piezoelectric actuators can be bonded on to frame before folding.

property	music wire	poly silicon	cuticle	resilin
Elastic Modulus $E \text{ Nm}^{-2}$	200×10^9	140×10^9	10×10^9	2×10^6
yield stress Nm^{-2}	4×10^9	0.7×10^9	0.4×10^9	
ultimate extension	2%	.5%	2-3%	300%
endurance limit Nm^{-2} ($> 10^6$ cycles)	10^9 0.5%	0.5%		
$Q = \frac{\pi}{\text{lossfactor}}$	200	10^4	30	> 100
density mg/mm^3	7.9	2.3	1.3	
wave velocity $\sqrt{\frac{E}{\rho}} (\text{ms}^{-1})$	5000	7800	2800	
reference	Oberg 88	Keller 98	Jensen 62	Jensen 62

Table 6: Material properties for thorax.

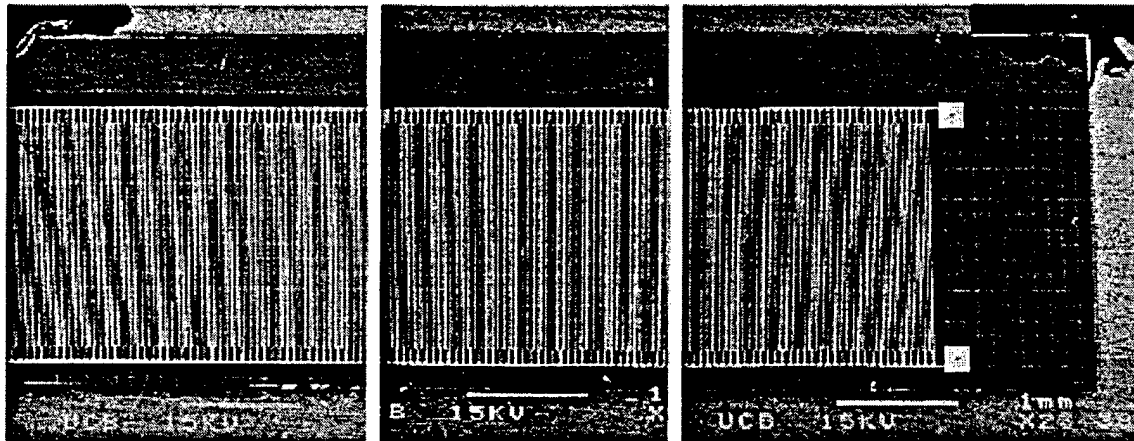


Figure 11: Prototype wing, 10 mm by 3 mm by 60 μm thick with integrated non-functioning solar cells and non-functioning force sensing piezoresistors.

3.1.1 Material Limits

Material limits for several thorax materials are given in Table 6. Note that peak stress must be limited to maintain life. This can be done both with thin materials, and by keeping the overall system Q low since high Q increases dynamic stresses. Stainless steel performance is expected to be similar to music wire in that the structural loss factor will not be significant compared to wing or actuator dissipation.

3.2 HEXSIL Wing Fabrication

Polysilicon (Hexsil) wings have been fabricated with integrated solar cells (Figure 11). The wings have a 5 μm face sheet, and reinforcing ribs approximately 60 μm thick. The density of the wing is approximately 10% of the density of polysilicon, for a mass per wing of about 0.4 milligram.

Solar cells in single crystal silicon were made for test purposes during the same fabrication run. The single crystal silicon solar cells are functional, with open circuit voltages in the 0.5 V range. Efficiency is still being characterized. The polysilicon solar cells did not work. This may have been due to improper diffusion of the P and N regions.

Our current effort is to fabricate a silicon-on-insulator (SOI) wing which will have better solar cell characteristics, with the current goal of 30 cells wired in series, with projected output of 10 volts open circuit voltage, and 0.2 to 0.3 mA short circuit current. The new wings will have a 20 micron thick single crystal solar cell which should have an efficiency of better than 10%, providing 100 microWatts per square millimeter in full sunlight. The support structure for the wing in this new design will be single crystal silicon as well.

Another set of wings will be fabricated with integral strain gauges, to measure wing forces during flight. To build the fan-fold style of wing, we anticipate using a thin, flexible polyimide backing strip between individual rigid silicon pieces, and then molding the wing into fan-fold configuration. The polyimide layer can contain flexible conductors as needed.

Initial experiments on the HEXSIL wing showed that it can survive the dynamic loading of the wing beat tester (Figure 12) at 60 Hz. However, the wings are quite fragile, and frequently broke during handling for assembly. For handling and mounting, we will use our vacuum pickup to reduce chances of damaging the parts.

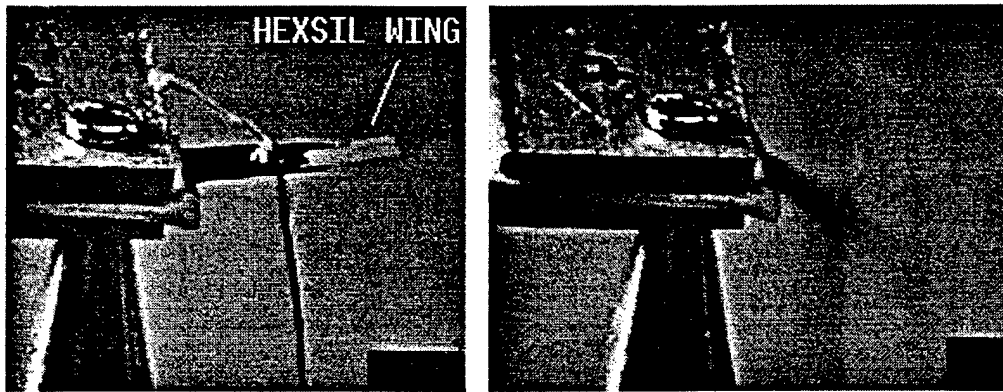


Figure 12: Hexsil wing mounted to wing test structure. Wing survived beating at 60Hz.

3.3 Piezoelectric Actuator Fabrication

Our current plan for the actuators is to use a unimorph structure, consisting of a $100\text{ }\mu\text{m}$ thick layer of piezo material bonded to a $100\text{ }\mu\text{m}$ thick stainless steel elastic backing layer, with the piezo material pre-stressed in compression. We plan to bond the piezo structure to the stainless steel thorax frame, after the frame has been folded. Two piezo actuators will be bonded onto each of the 4 thorax frames, for a total of 8 actuators. Initial fabrication experiments have bonded $2\text{ }\mu\text{m}$ thick PLZT to $12\text{ }\mu\text{m}$ stainless steel. We are pursuing both PLZT fabrication and polishing down PMN-PT materials to get the desired $50 - 100\text{ }\mu\text{m}$ thickness needed for the unimorph.

The relatively small strains associated with the converse piezoelectric effect can be mechanically amplified by joining a thin piezoelectric layer to an elastic support, thus displacing the center of bending from the midplane of the piezoelectric layer. Such benders are available commercially in bulk form. To fabricate analogous actuators at the MFI scale (each layer several microns thick), we are adapting the Laser Liftoff process developed at Berkeley to assemble novel unimorph microactuators. The ceramic piezoelectric films (PZT or PMN-PT) are first deposited onto sapphire or MgO substrates that are ideally suited to the deposition of the highest quality thin or thick films. The structure is bonded, film-side-down, to the elastic support (in this case, a stainless steel shim). The final step is to separate the sapphire or MgO substrate by excimer laser irradiation through the transparent substrate. A single $30\text{--}40\text{ ns}$ pulse at 500 mJcm^{-2} is sufficient to debond the piezoelectric film from the growth substrate, resulting in a thin-film unimorph actuator structure. The first demonstration of this process was completed. A detailed description of the experiment is provided below.

PZT films were obtained from NZ Applied Technologies, Inc. Thick PZT films (2 to 10 microns) were grown on sapphire substrate using their proprietary metal-organic decomposition (MOD) method. On the sapphire substrate, a thin layer of PbTiO_3 was deposited first as the sacrificial layer to facilitate separation for it is relatively easier to decompose than PZT. Conductive oxide $(\text{La}, \text{Sr})\text{CoO}_3$ ($\approx 100\text{ nm}$) layers were used as electrodes for the PZT film. The complete heterostructure had the layer sequence: LSCO/PZT/LSCO/PT on sapphire.

A transient-liquid phase Pd-In bonding technique, developed at Berkeley, was utilized for low-temperature bonding. Ti (6 nm)/Pd (100 nm) bilayers were deposited by electron gun evaporation onto both the PZT heterostructure and a polished stainless steel shim of 25 micron thickness. An In layer of thickness 1 micron was then thermally evaporated onto the Pd-coated PZT. During pressure bonding at 200° , the In melts and flows laterally to fill voids and accommodate surface roughness. At the same time, a solid phase reaction to form the PdIn_3 intermetallic is initiated

and proceeds to completion, consuming the molten In. The result is a strong metallic bond consisting of a phase with a melting point above 600° .

Laser lift-off was performed using a Lambda Physik Lextra KrF excimer laser (wavelength $\lambda = 248nm$, pulse duration $\tau = 38ns$). At this wavelength, the sapphire substrate is transparent while PT and PZT are strongly absorbing, with an absorption length on the order of 20 nm. As a result of the short pulse length and the low thermal conductivity of the PZT, the thermal diffusion length is also very short ($< 150nm$). Consequently, heating is highly localized to the interface. Separation is achieved at a fluence of $400mJcm^{-2}$, corresponding to an estimated temperature (based on thermal modeling) $> 1300^{\circ}$.

For this demonstration, a sample area of about $4mm^2$ was successfully transferred to the steel shim. The surface of the lifted-off film is uniform and smooth. X-ray diffraction revealed that the liftoff process did not alter the perovskite phase, except that the rocking curve peak widths were broadened slightly, indicative of some stress relief.

Top Pt/Ti electrodes ($50\mu m$ in diameter) were made using the photoresist lift-off method. Basic ferroelectric properties were studied using a RT66A ferroelectric testing system (Radiant Technologies). Although the films were found to be electrically leaky before liftoff, these preliminary results confirm that the liftoff process did not substantially alter the ferroelectric properties.

We are pursuing both PZT and PMN-PT actuators, with PZT actuators for initial experiments, as it is more readily fabricated, and PMN-PT for the final material. (PMN-PT is more compliant, has higher piezoelectric coefficients, and a higher strain limit, giving higher power density than PZT). Thin-film PZT materials have been fabricated in our Microlab by the sol-gel process, and are currently undergoing testing. As discussed above, the MFI thorax is envisioned as a folded flexural structure with bonded piezo actuators. Work is in progress to bond thin-film PZT actuators to $12\mu m$ thick stainless steel, as an initial model of thorax/actuator combination.

Sands is working with NZ Applied Technologies to fabricate PMN-PT single crystal films on magnesium oxide wafers. The PMN-PT actuators will be bonded to our thorax structure, and then removed from the MgO substrate using a laser lift-off process.

4 Aerodynamics and Wing Control

To understand necessary kinematics and control for lift and thrust generation, we have been studying flow fields around real flies, a large mockup (Robofly) in oil, and an at-scale mockup wing using Particle Image Velocimetry (PIV).

4.1 Flow Visualization of Insects

We have started initial measurements of the wing-induced flow around *drosophila* (Figure 13) and *calliphora* (Figure 14). Fruitflies are steadier fliers than blow flies and will allow us to capture flight data more easily. We will also be able to compare any differences in flow fields due to scaling or kinematic differences between the insects. We installed a camera and lasers on a vibration isolated table to obtain jitter free images of *drosophila* flight, and obtained adequate resolution to see shed vortices in the flow. In the next quarter, we will be using a wing beat analyzer to capture a detailed sequence of images during the wing cycle.

4.2 RoboFly

The RoboFly apparatus, which consists of a two-winged system which can closely mimic the stroke kinematics of a fruit fly, (or other arbitrary kinematics) was successfully run in its oil tank.

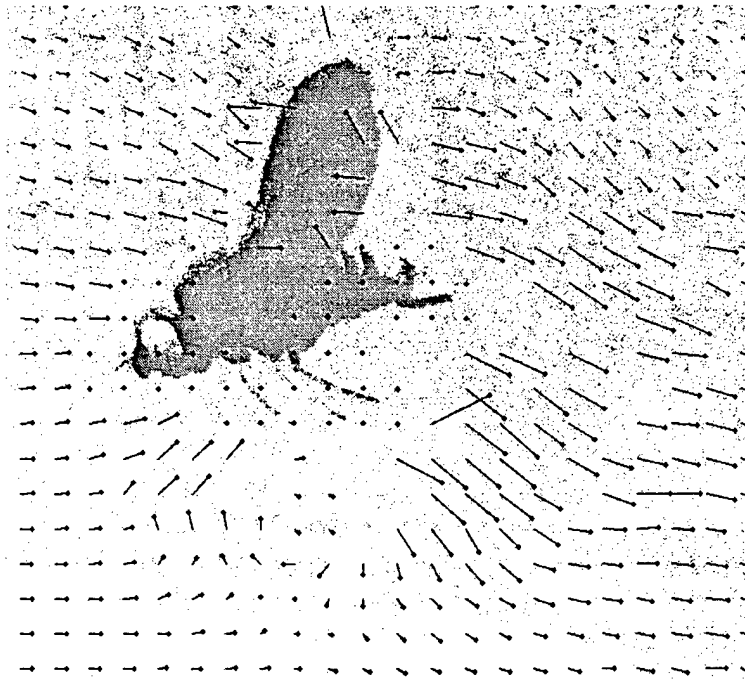


Figure 13: Flow structures measured using PIV for *Drosophila*, with head wind speed of $0.5m\ s^{-1}$ and peak induced velocity of $2m\ s^{-1}$.

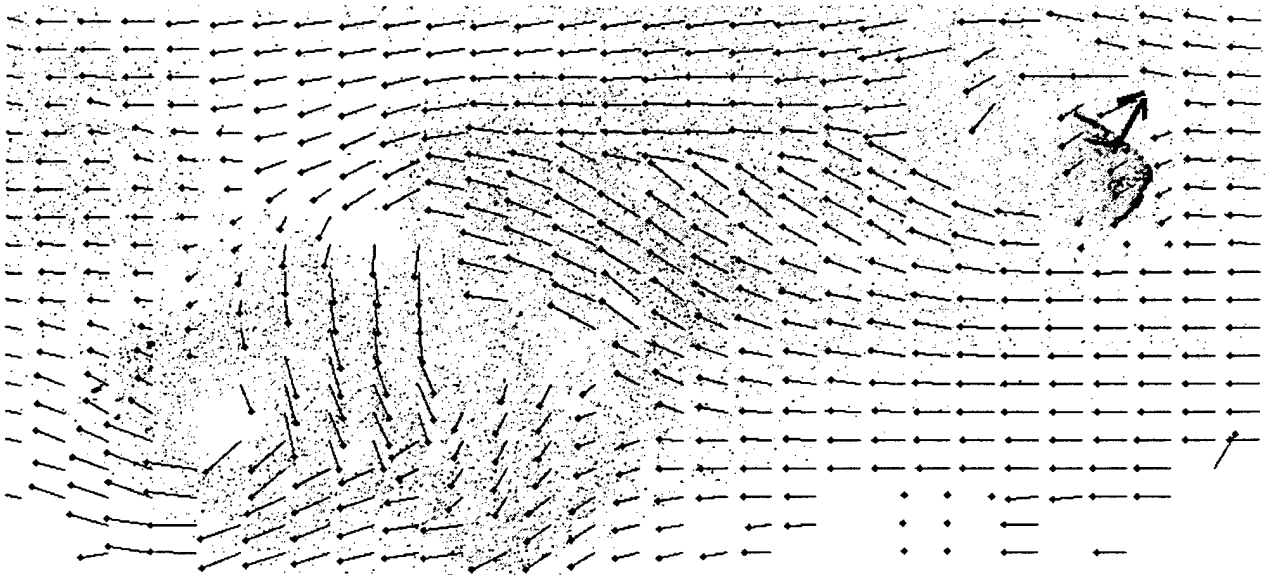


Figure 14: Flow structures measured using PIV for *Calliphora*, with head wind speed of $3m\ s^{-1}$ and peak induced velocity of $8m\ s^{-1}$.

Wing strain gauges are used to measure instantaneous wing forces, and the integral of forces around a closed wing beat cycle can be measured to determine net flight forces. (This approach will also be used on the MFI mockup to estimate flight forces). Each wing is driven by 3 stepping motors, and wing kinematics are under programmable control. Flow was visualized using air bubbles in the oil tank and PIV.

We have collected image and vector data on shed vortices at the bottom of the downstroke, vortices produced during the squeezing of the wings together at the top of the upstroke and the leading edge bubble that is produced during reattachment of the leading edge vortex (Figure 15). In a result anticipated for many years by many insect flight scholars, Dickinson and Lehmann have found wing trajectories which generate peak lift forces of four times the equivalent insect weight. The timing of an equivalent of a back spin motion at the bottom of the wing stroke can change the net lift from positive to negative. The second key finding is the significant forces generated by wake capture at the top of the stroke. This is a very important result, as it appears that we now to have a basic understanding of sufficient wing stroke parameters for flight, a long-standing open question. In addition, we have an initial trajectory from which to optimize, to minimize required wing rotation, for example.

The hoverfly wing kinematics are of interest because the hoverfly uses a stroke pattern with less wing rotation than *drosophila*. Measurements of flight forces have been made using robofly for the hoverfly kinematics (Figure 16).

Although clap and fling (wings meeting at top of stroke) has been theoretically proposed as a lift generation mechanism for some insects, lift forces have not previously been quantified. Flow visualization and force measurements with Robofly (Figure 17) found a 10% force augmentation when the wings clap. This is a relatively small effect, and hence we can safely neglect it in the MFI design, simplifying required kinematics, and avoiding possibly damaging collisions between wings.

4.3 Thorax/Wing Mockup

We built an MFI mockup using 2 voice coil actuators (VCA) per wing (Figure 18) driven by servoamps. A closed loop position control system using optical position sensors allows tracking of a sinusoid at 80 Hz without resonance of the system. We expect to be able to drive flexural thorax structures at greater than 100 Hz using a resonant mode.

We completed an initial prototype for a 2 degree of freedom mechanical flapper, with position control of the attached wing. The wing gives adequate deflection and rotation at low frequency. This thorax was one of the simplest designs possible— an 'L'-shaped piece of $50\mu\text{m}$ spring steel, whose lengths have been appropriately chosen for the desired application. Unfortunately, this design exhibited a tendency to fail before 400,000 cycles have been completed at 60 Hz due to the large induced strains, cracks and rough edges. We will be replacing the 'L' structure with the flexural 4 bar mechanisms described in Section 3.1 to improve wing stroke and rotation, as well as to test the flexural structures for any lifetime problems.

We have started initial comparisons of the wing-induced flow around *calliphora* with the flow around our mockup flapper. Figure 19 show the measured flows using our PIV system and a one degree of freedom flapper.

4.4 Control and Integration

Control and stabilization of the MFI is just starting, as the main effort in the first year has been in structural design and analysis, as well as understanding the underlying aerodynamics. An

figure 4

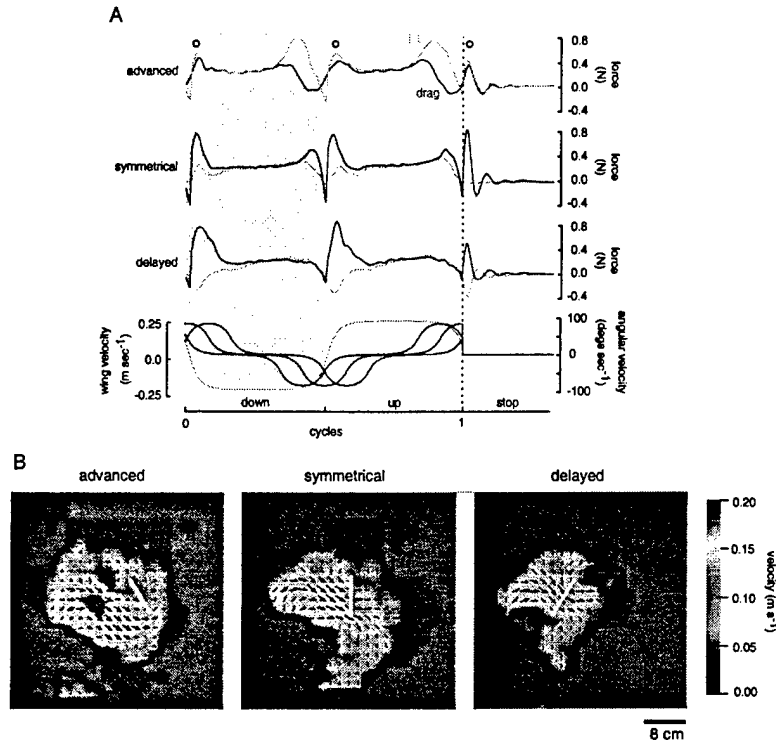


Figure 15: Evidence for wake capture at the end of each half stroke. (A) Lift (red) and drag (blue) are plotted for one continuous cycle preceding a complete stop at the end of the upstroke. When wing rotation is advanced, the wing develops lift and drag peaks that develop after translation has ceased. When wing rotation is symmetrical and stops in a vertical position, the post-translation force is pure drag with no lift component. When rotation is delayed, the wing generates negative lift at the end of translation. The rising phase of the post-translational transients is similar to that of the force transients at the start of each half-stroke during continuous flapping (white dots). (B) Flows through the mid-chord of the wing (white bar) immediately prior to complete stop. Arrow lengths and direction indicate magnitude and orientation of local fluid velocity. Fluid velocity is also indicated by pseudocolor background. While the gross orientation of the flow is similar in all three cases, the flow velocities are greater when rotation is advanced, consistent with the occurrence of stronger rotational circulation generated and subsequently shed during the upstroke.

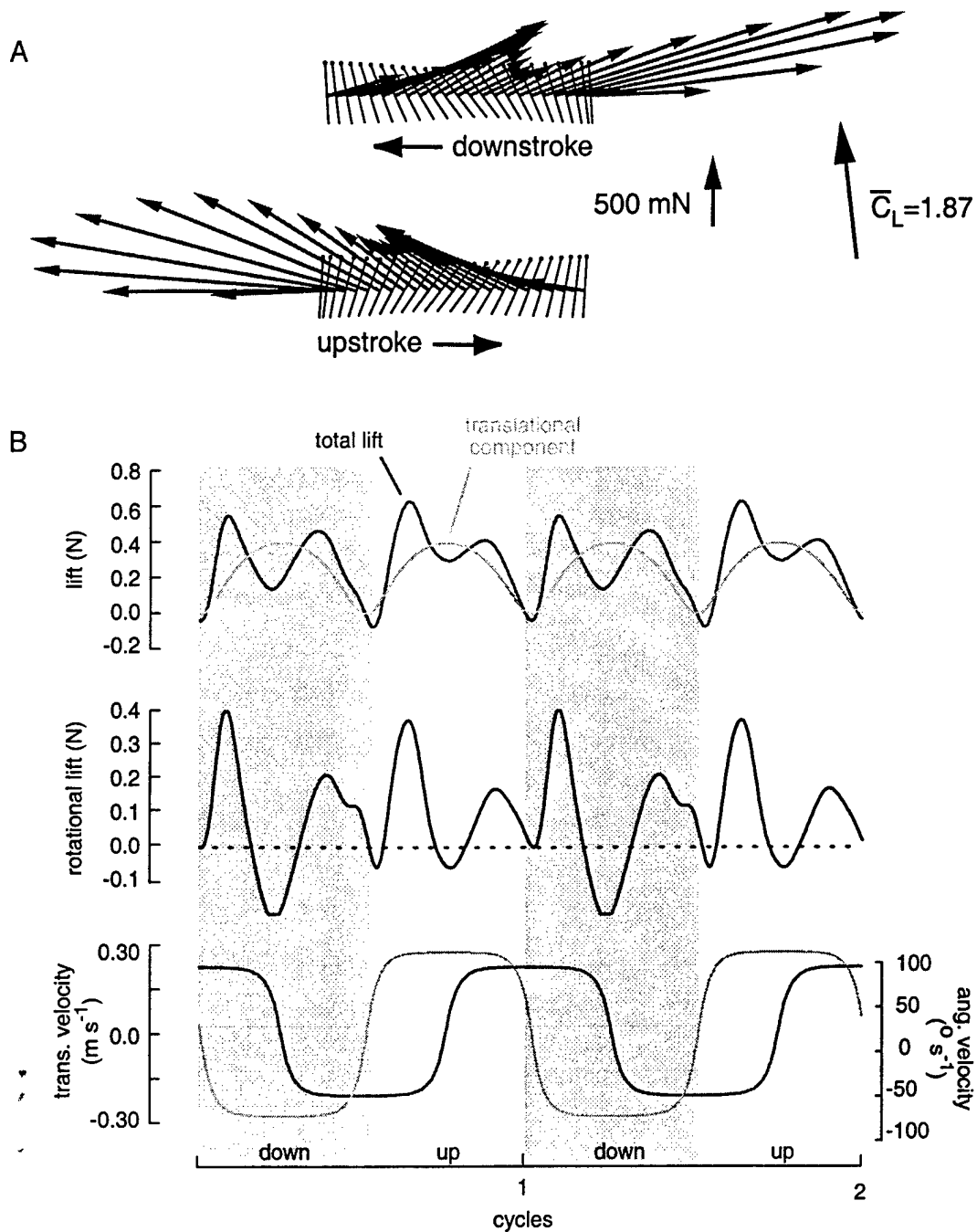
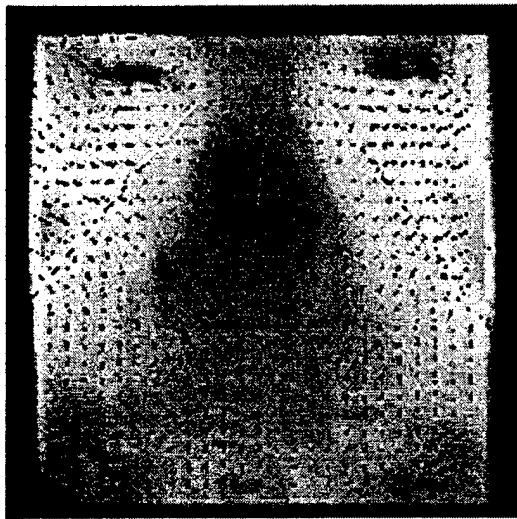
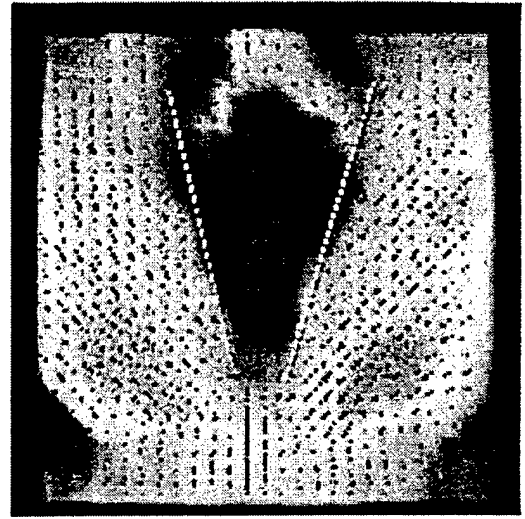


Figure 16: Forces generated by a kinematic pattern based on the wing motion of hoverflies. (A) Instantaneous force vectors superimposed on a diagram of wing motion (stroke amplitude = 69°, frequency = 0.402 mHz, angle of attack at mid-stroke = 50° for both upstroke and downstroke). (B). Time history of measured rotational (red) and translational estimates (blue) of lift, rotational lift, and kinematic velocities.



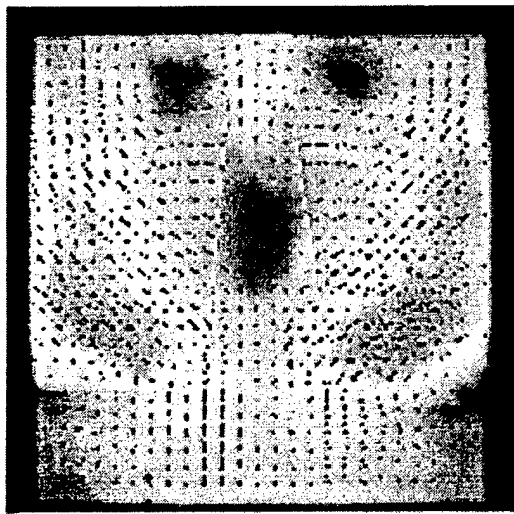
- 350 ms

A



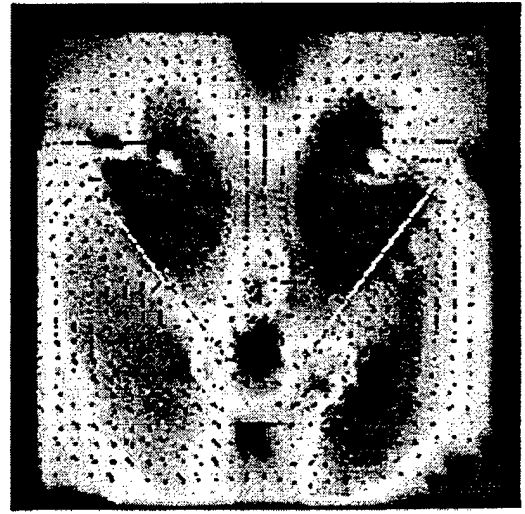
+ 100 ms

C



0 ms

B



+450 ms

D

Figure 17: Front view of robofly during clap and fling, with clap occurring in Frame B. There is a developing stagnation region immediately preceding the clap, caused by an outward flow field generated as the clapping wings exclude the fluid between them.

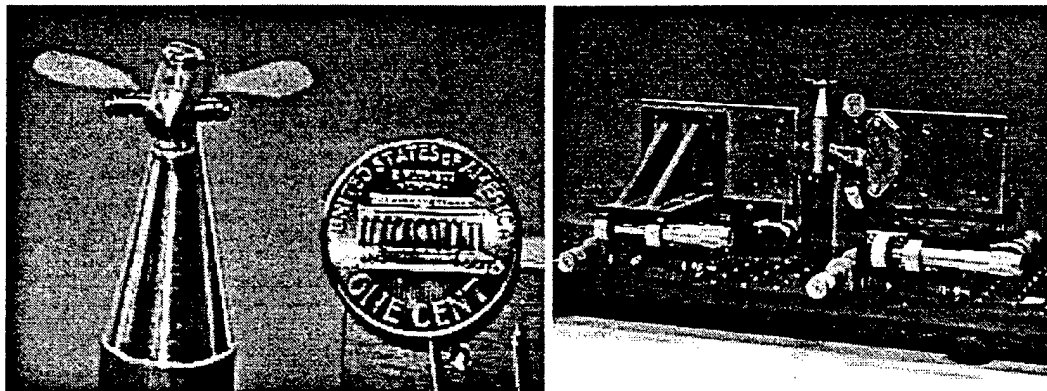


Figure 18: Insect mockup and wing tester using voice coil actuators.

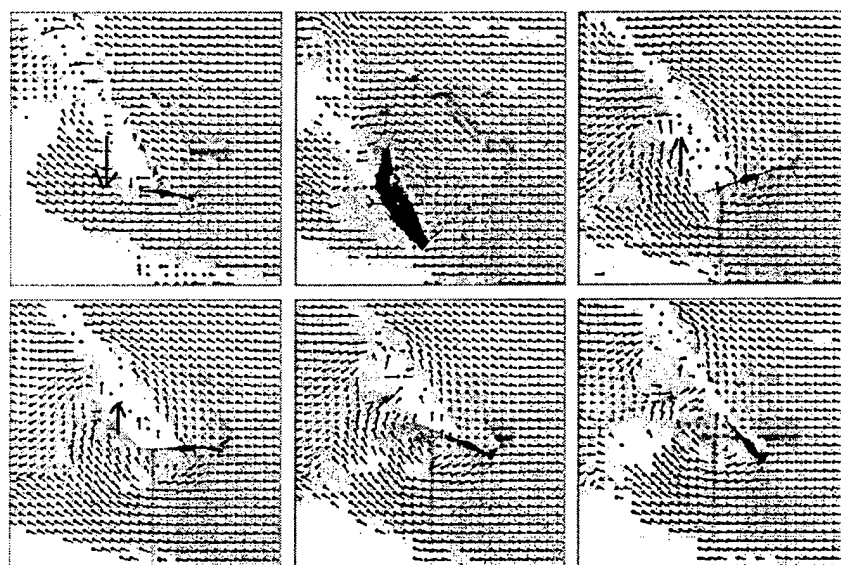


Figure 19: Flow pattern for at-scale mockup flapper. The flapper used in this experiment was running at 60 Hz, and induced peak flow velocities of $4ms^{-1}$. The one degree-of-freedom flapper does not yet have the necessary rotation to generate the wake pattern seen in *Calliphora* but we expect to see similar patterns using the 2 DOF mockup.

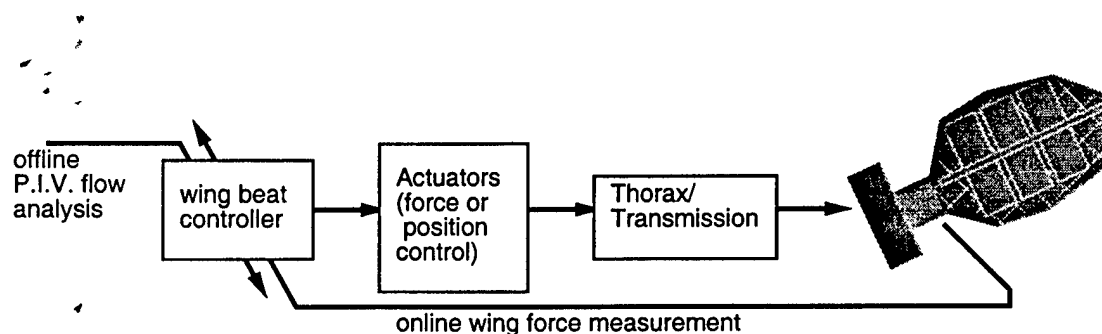


Figure 20: Wing control system overview.

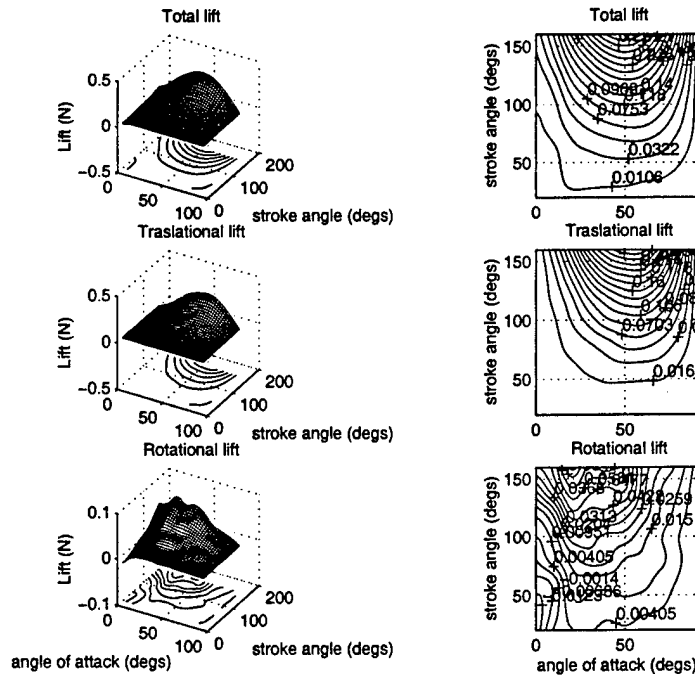


Figure 21: Mean lift maps: total (top), translational component (middle), rotational component (bottom). (Data from Robofly experiments).

overview of the wing control system is shown in Figure 20. We have used Robofly PIV data to start developing a model of flight forces as a function of stroke angle and angle of attack. Using a horizontal stroke plane, with symmetrical upstroke and downstroke, we measured flight forces for angle of attack from 0 to 90 degrees and stroke angle from 20 to 160 degrees. Results in the form of a *mean lift map* are shown in Figure 21. The optimal angle of attack was approximately 45 degrees. We intend to use the lift map for choice of kinematic patterns in design of the MFI, and to control flight forces by adjustment of wing stroke angle and angle of attack.

For the flight control system (Figure 22), simple optical flow algorithms were implemented in hardware using field programmable gate arrays by students in a digital design class taught by Fearing. Good results were obtained using simple difference algorithms and maximum tracking. Initial discussions with Samsung about using their single chip gyros on the MFI look promising, as their device is small ($1mm^2$).

5 Research Plan for Year 2

The overall plan for the MFI project is shown in Figure 23. Our main efforts in Year 2 will be testing the flexural 4 bar thorax driving a wing in the wind tunnel, while measuring forces and fluid flow using PIV. A detailed plan is given below.

5.1 Thorax Design

1. Develop masks and jigs for folding flexural 4 bar frames at-scale.
2. Develop fixtures for folding and bonding small stainless steel sheets.
3. Attach unimorph actuators and wings to folded structures.

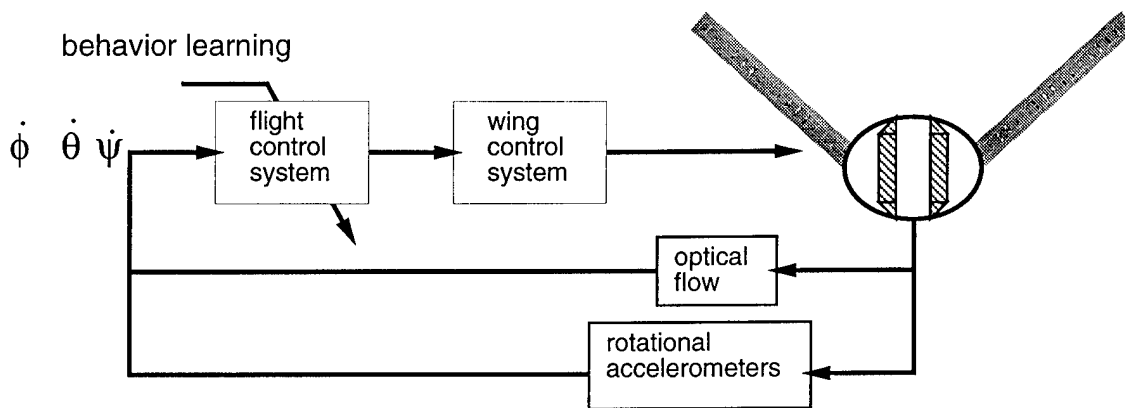


Figure 22: Flight Control System Overview

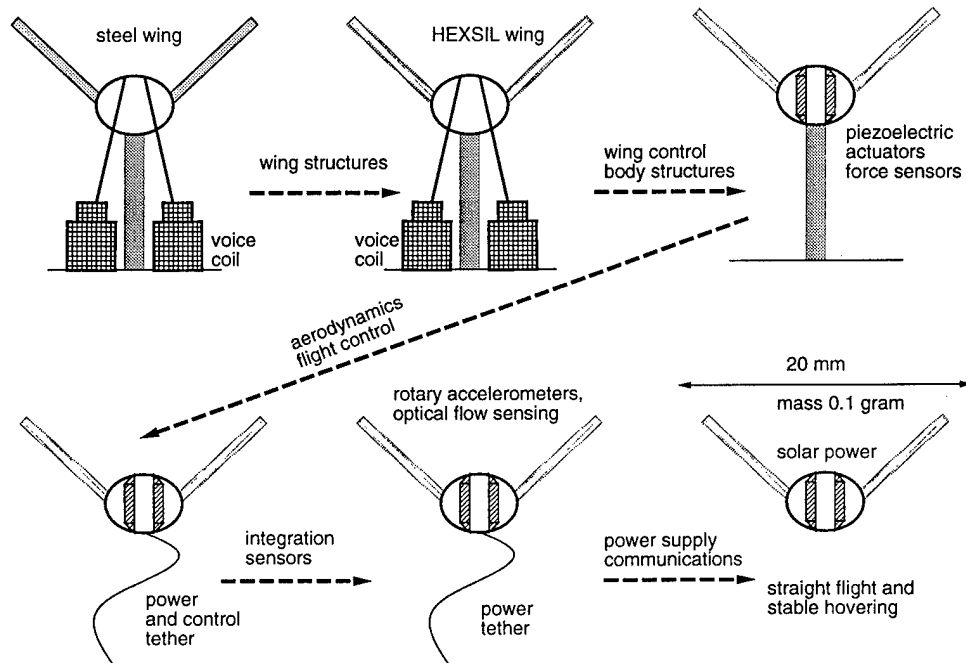


Figure 23: Overview of Research Plan for MFI Project

4. Test thorax and wing for adequate stroke, rotation, and lifetime with piezo actuation.

5.2 Wing Fabrication

1. Continue fabrication of wings with improved solar-cells.
2. Fabricate polysilicon wings with working force sensors for flight force measurements.
3. Develop process for fan-fold wings using polyimide layer with polysilicon wing segments.

5.3 Piezoelectric Actuation

1. Repeat demonstration using piezoelectric heterostructures with desired ferroelectric and piezoelectric properties (prepare results for publication).
2. Demonstrate fabrication of epitaxial piezoelectric bimorphs using the laser liftoff process. Epitaxial films, especially those with relaxor compositions, are predicted to be capable of strain levels exceeding 1% (compared to $\approx 0.1\%$ for polycrystalline films).
3. Develop appropriate mask-sets and patterning processes for fabrication of unimorph microactuators.
4. Characterize d_{31} -mode unimorph deflection for these microactuators; compare with predicted deflection and experimentally observed behavior of commercial benders.
5. Incorporate experimental data on microactuators into models of MFI propulsion systems; optimize microactuator structures accordingly.

5.4 Flow Visualization of Insects

1. Record PIV data from fruitfly and blowfly wing stroke sequence, and determine significant differences between flow patterns, if any.
2. Analyze leading edge vortex and wake capture for fruit fly and blowfly.

5.5 Robofly

1. Find and characterize wing trajectories which minimize peak forces and peak power while maintaining sufficient lift and thrust forces.
2. Explore other insect wing kinematics.
3. Apply learning control techniques to optimize wing trajectories. Are fruit fly kinematics already optimal?

5.6 Thorax/Wing Mockup Control

1. Using VCA setup, drive flexural structure and fan fold wing at 100-150 Hz to test durability.
2. Measure forces on polysilicon wing with integral force sensors.
3. Visualize flow of fan-fold wing, and control wing rotation to control flight forces.
4. Develop flight force map as function of stroke and rotation for learning control.